DESIGN OF AN EDUCATIONAL EXPERIMENTAL PLATFORM FOR MULTI-SOURCE FUSION LOCALIZATION IN ROBOTICS BASED ON AN ADAPTIVE EKF
/
基于自适应 EKF 的机器人多源融合定位教学实验平台设计

Yi ZHOU [1], Xiaofan LIU [2], Ruiqi WANG [3], Jinhong ZHANG [4], Pengcheng LV [5,*]
[1] Applied Technology College of Soochow University, Soochow, China;
[2] Communication University of China, School of Economics and Management, Beijing, China;
[3] Beijing Institute of Technology, School of Design and Art, Beijing, China;
[4] Qingdao University of Technology, School of Civil Engineering, Qingdao, China;
[5] Ocean University of China, College of Engineering, Qingdao, China;
Tel: +86 13964379460; E-mail: lvpengcheng@stu.ouc.edu.cn
Corresponding author: Pengcheng Lv
DOI: https://doi.org/10.35633/inmateh-78-104

Keywords: *Multi-source fusion positioning; 3D LiDAR; GNSS-RTK; Feature extraction*

ABSTRACT
To address the challenges posed by severe canopy obstruction in orchards and complex terrain—conditions under which single-GNSS systems frequently lose signal lock, as well as the susceptibility of single-sensor systems to dynamic interference—this paper proposes a multi-source fusion positioning framework based on an adaptive extended Kalman filter (AEKF), integrating GNSS-RTK and 3D LiDAR. To overcome the issue of sparse and discontinuous point cloud features in agricultural environments, a ground segmentation method based on a concentric zone model combined with an improved RANSAC algorithm is developed. This approach enables high-frequency and accurate extraction of orchard row geometric features under complex conditions, including muddy ruts and dynamic human interference, thereby establishing reliable observational constraints for local relative pose estimation. An adaptive observation noise covariance adjustment mechanism based on signal confidence is further proposed. By continuously monitoring RTK quality indicators and accuracy metrics in real time, the system dynamically suppresses unreliable state updates during periods of GNSS signal degradation and seamlessly switches to an error compensation mode based on lateral and heading constraints derived from 3D LiDAR. This effectively mitigates cumulative drift associated with dead reckoning. Experimental results demonstrate that, under challenging conditions involving intermittent canopy gaps and dynamic occlusions, the proposed system achieves a root mean square error (RMSE) of 0.042 m for lateral positioning over the entire trajectory, while the heading RMSE is maintained within 1.85°. The proposed approach effectively addresses the problem of intermittent localization loss in complex orchard environments, providing a robust state estimation framework that enables agricultural robots to operate without reliance on prior mapping, while supporting high-precision global path planning and real-time local obstacle avoidance.

摘要
针对果园树冠严重遮挡与复杂地形导致单一全球导航卫星系统易失锁，以及单一感知手段易受动态干扰的难题，本文提出了一种基于自适应扩展卡尔曼滤波的 GNSS-RTK 与 3D 激光雷达多源融合定位框架。针对农业环境点云特征离散的问题，设计了基于同心区模型的地面分割及改进的 RANSAC 算法。该算法能够在泥泞车辙和动态人员干扰等复杂工况下，实现果树行几何特征的高频精准提取，从而构建局部相对位姿的观测约束。提出了一种基于信号置信度的自适应观测噪声协方差调整机制。系统通过实时监测 RTK 质量标志位与精度因子，在 GNSS 信号退化阶段自适应阻断不可靠状态更新，并无缝切换至基于 3D 激光雷达侧向与航向约束的误差补偿模式，有效抑制了航位推算中的累积漂移。实验结果表明，在存在连续缺株与动态遮挡的严苛条件下，系统全过程横向定位均方根误差 RMSE 仅为 0.042m，航向偏差 RMSE 被严格控制在 1.85°以内。本研究有效克服了复杂果园环境中的"定位盲区"问题，为农业机器人摆脱预建图依赖、实现高精度的全局路径规划与实时局部避障提供了高鲁棒性的状态估计基础。

INTRODUCTION
The autonomous operation of orchard robots relies on high-precision, highly robust navigation and positioning systems; furthermore, the underlying system must provide stable and continuous pose estimation without relying on pre-built high-precision global maps *(Gao et al., 2021)*. Sensors struggle to cope with the complex environment of orchards: GNSS-RTK is prone to carrier phase loss under tree canopy cover, resulting in a sharp drop in positioning accuracy; wheel odometers are highly susceptible to slippage on uneven, muddy

ground, leading to diverging errors; whilst 3D LiDAR (LiDAR) point cloud registration over long distances not only places a heavy computational load on the system but also suffers from significant cumulative drift issues *(Jiang et al., 2022)*.

Existing multi-source heterogeneous sensor fusion technologies (such as Extended Kalman Filtering, EKF) still face two major bottlenecks in orchard applications: firstly, the difficulty of efficiently and robustly extracting stable navigation features from cluttered agricultural point clouds (such as weeds and moving personnel); secondly, traditional algorithms typically employ a fixed observation noise covariance matrix; consequently, when GNSS signals undergo sudden changes or are unavailable for extended periods, the filter is highly susceptible to system divergence due to over-reliance on erroneous observations or reliance solely on odometry estimates *(Lv et al., 2025)*.

In response to the aforementioned challenges, this paper proposes a multi-source fusion positioning framework based on adaptive EKF, integrating GNSS-RTK and 3D LiDAR data, to provide robust state feedback for global path planning and real-time obstacle avoidance. The main contributions of this paper are as follows:

1) A robust algorithm for tree-row feature extraction and relative localisation that does not rely on a global map has been proposed: for complex agricultural point clouds, a mechanism for extracting regions of interest and filtering out ground points has been designed, and an improved RANSAC algorithm has been employed for tree-row line fitting. This effectively overcomes interference from weed noise, missing plants and dynamic obstacles, enabling real-time calculation of high-frequency lateral and heading deviations.

2) Design of an adaptive mode-switching and error compensation mechanism based on signal confidence: by analysing RTK quality flags and the Doppler error (DOP) in real time, the observation noise covariance matrix is dynamically adjusted. During periods of GNSS signal degradation, invalid observations are adaptively filtered out, and the system seamlessly switches to a compensation mode combining odometry and tree-line geometric constraints, thereby effectively suppressing the divergence of the position estimation.

3) System-level field validation was successfully completed in a real-world orchard environment: a tracked validation platform was deployed in a standardised vineyard with 3-metre row spacing and 1.5-metre plant spacing. The experiments demonstrated that, even under demanding conditions such as muddy ruts, dynamic human interference and continuous gaps between plants, the system maintained centimetre-level lateral positioning accuracy and exceptional heading stability, achieving highly robust positioning that relies on satellites for macro-level guidance and on the environment for micro-level guidance.

MATERIALS AND METHODS

GNSS-RTK Measurement and Coordinate Mapping

Conventional single-point GNSS positioning relies on pseudorange measurements and is subject to factors such as satellite ephemeris errors, ionospheric delays and tropospheric delays; as a result, its accuracy is typically in the metre range, which fails to meet the requirements for centimetre-level precision work between rows in orchards. In order to obtain high-precision prior information on the absolute pose of a robot in an orchard environment, this study developed a measurement system based on dual-antenna GNSS-RTK. By incorporating differential observations between the reference station and the rover, the system utilises carrier phase observations to efficiently eliminate errors *(Nie et al., 2021)*.

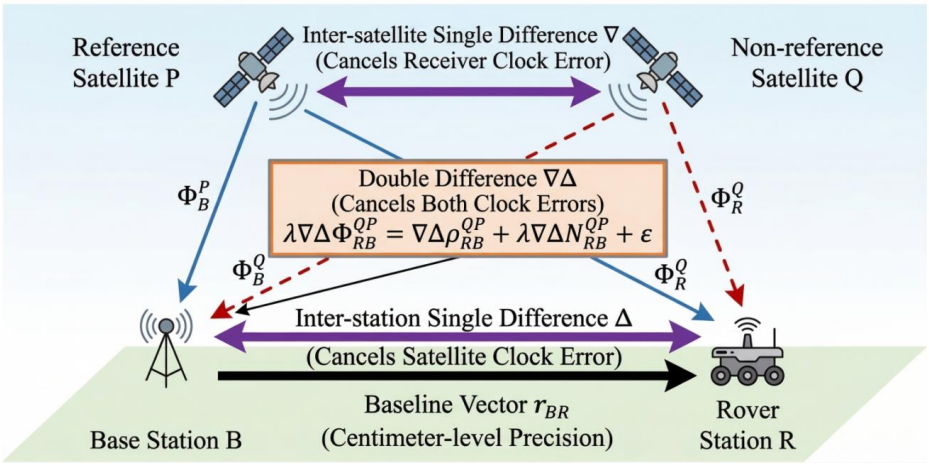

Fig. 1 – Schematic Diagram of GNSS-RTK Carrier Phase Double-Differential Positioning

The dual-antenna GNSS direction-finding system developed in this study comprises a master antenna (Master) and a slave antenna (Slave), both rigidly mounted on the central axis of the robot chassis, with a baseline length of $L = 1.0m$. The system utilises a carrier phase double-difference model in combination with the LAMBDA integer ambiguity resolution algorithm to mitigate common error sources, including satellite clock errors, receiver clock errors, and atmospheric delays *(Pire et al., 2017)*.

Dual-antenna direction finding is essentially a relative positioning problem based on a moving baseline. In this configuration, the master antenna serves as a temporary reference station, while the slave antenna acts as a rover. Through RTK processing, the baseline vector $r_{ms} = (\Delta x_{enu}, \Delta y_{enu}, \Delta z_{enu})^T$ between the slave antenna and the master antenna can be estimated. Based on this baseline vector, the robot's heading angle φ and pitch angle θ can be determined, as illustrated in Figure 2.

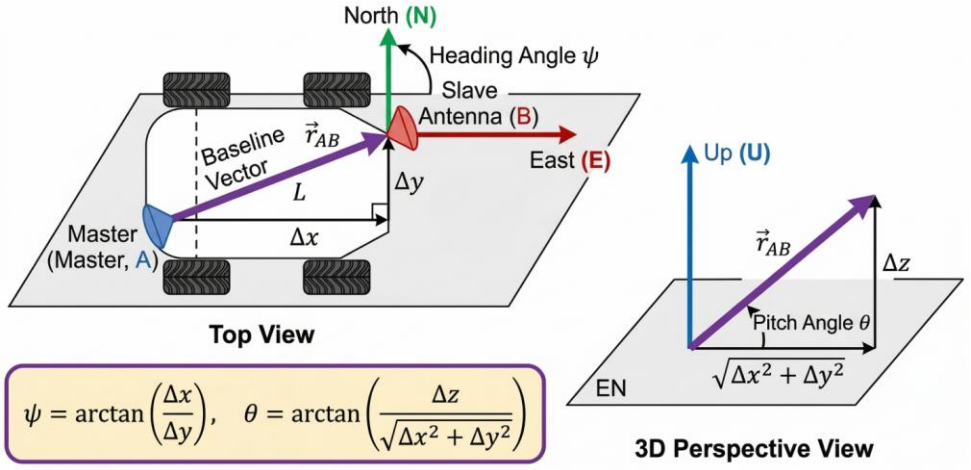

Fig. 2 – Geometric model of dual-antenna GNSS-based heading and pitch estimation

The raw data output by the GNSS receiver consists of geodetic coordinates (λ, ϕ, h) based on the WGS-84 ellipsoid model (longitude, latitude, ellipsoidal height); however, as the robot's path planning and motion control are both performed in a local Cartesian coordinate system, it is essential to establish a rigorous spatial projection transformation model *(Qin et al., 2024)*. In this study, WGS-84 coordinates were first converted to the Earth Centre-Eastern Europe (ECEF) coordinate system, and then, using rotation and translation matrices, strictly projected onto a local Northeast-West (ENU) secant plane rectangular coordinate system with the fixed control point at the orchard entrance as its origin *(Rösmann et al., 2015)*. Through transformation, the system maps non-linear latitude and longitude data into metric Euclidean coordinates, providing standardised state inputs for the subsequent adaptive extended Kalman filter *(Qiu et al., 2020)*.

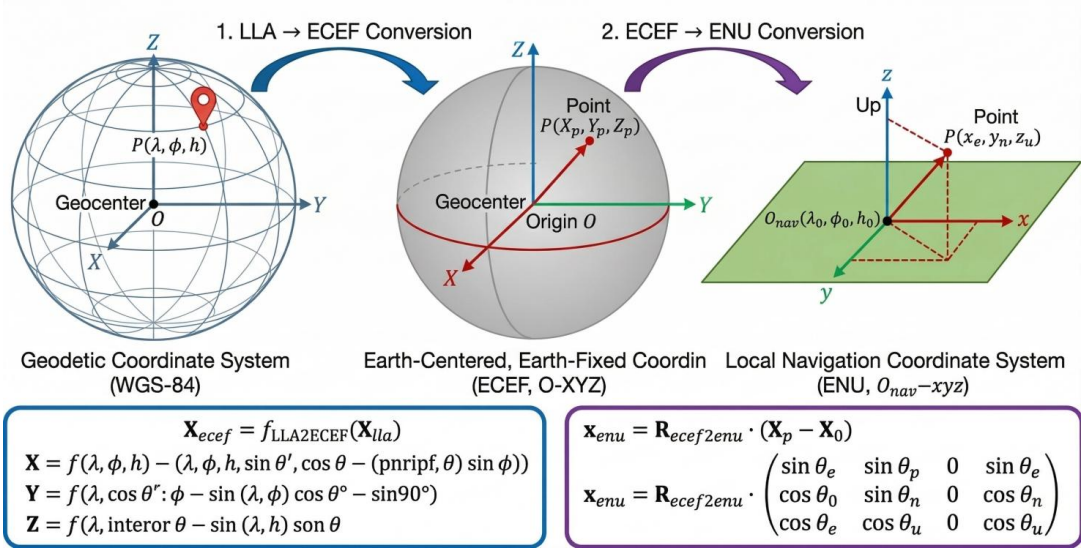

Fig. 3 – Schematic Diagram of Multi-Coordinate System Spatial Transformation and Projection Relationships

LiDAR-Based Relative Pose Estimation via Robust Tree Row Extraction

To meet the real-time requirements of navigation systems (which are typically necessary $> 10\text{Hz}$), the scale of point cloud processing must be reduced by using a pass-through filter to extract the region of interest (ROI), thereby effectively removing interfering data outside the navigation area. Let the original point cloud be denoted by P_{raw}, and the pre-processed point cloud set be denoted by P_{roi}:

$$P\_roi = \{p\_i \in P\_raw \mid 0 \le x\_i \le L\_view, |y\_i| \le W\_aisle, h\_\min \le z\_i \le h\_max\} \quad (1)$$

In the formula, L_{view} represents the forward line-of-sight distance, W_{aisle} represents the half-line-width threshold, and h_{min} and h_{max} represent the lower and upper limits of the cropping height, respectively *(Shan et al., 2018)*. Using a surface-fitting segmentation algorithm based on the concentric zone model, P_{roi} is divided into a ground point set P_{ground} and an obstacle point set P_{obs}. A KD-tree spatial index is constructed to accelerate the nearest-neighbour search, and the spatial centroids of the effective tree clusters are calculated as feature points $T_j(x_j, y_j)$:

$$x_j = \frac{1}{N_j \sum_{p \in c_j} p_x}, y_j = \frac{1}{N_j \sum_{p \in c_j} p_y} \quad (2)$$

The feature points y extracted are divided into a set of points on the left branch and a set of points on the right branch based on their coordinates *(Wu et al., 2021)*.

Due to measurement errors and irregularities in trunk growth, the set of extracted feature points is not strictly collinear and may contain a small number of outliers; therefore, the highly robust RANSAC algorithm is employed for line fitting. Construct a 2D line model $ax + by + c = 0$ *(Xue et al., 2023)*. In each iteration, two points are randomly selected from the point cloud to calculate the model parameters. The algebraic distance from the remaining points to the line is then calculated; if the distance is less than the threshold (set at 0.15 m), the point is classified as an interior point *(Yang et al., 2022)*. After the K iteration (where $K = 100$ is chosen in this system), the model containing the largest number of interior points is selected as the optimal tree-line. This yields the following:

Left-hand side of the tree equation:L_{left}: $a_L x + b_L y + c_L = 0$;

Right-hand side of the tree equation:L_{right}: $a_R x + b_R y + c_R = 0$

To ensure that the robot travels along the centre of the working row, a central navigation path L_{mid} is generated based on the fitting results of the left and right rows *(Yang et al., 2015)*. Given that the left and right rows may not be strictly parallel, the centre line equation $ax + by + c = 0$ is derived by taking the weighted average of their parameters *(Zhou et al., 2014)*:

$$A = \frac{a_L + a_R}{2}, B = \frac{b_L + b_R}{2}, C = \frac{c_L + c_R}{2} \quad (3)$$

This centre line serves as the ideal reference for the robot's relative navigation.

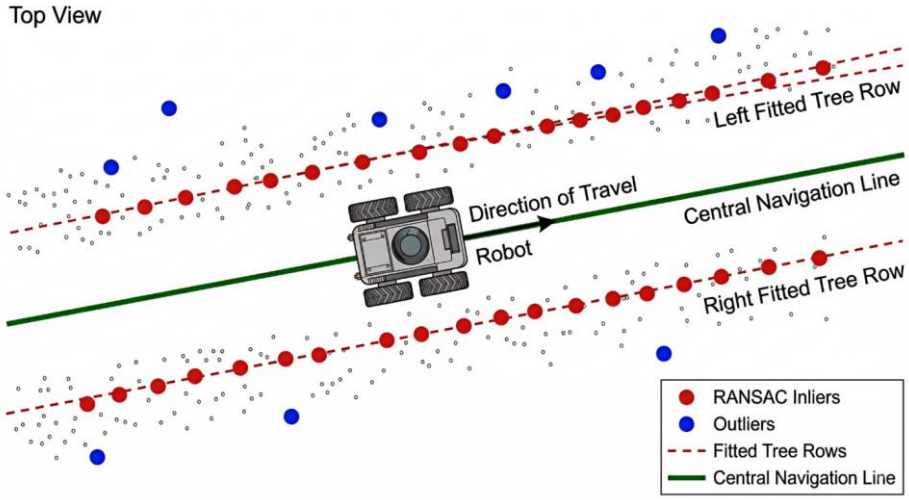

Fig. 4 – Schematic Diagram of Centre Extraction and Linear Fitting for Tree Trunks

Defining the origin of the robot's body coordinate system as $O(0,0)$, with the robot's head facing the X-axis, allows for the real-time calculation of the robot's relative positional and orientational deviations *(Zhou et al., 2021)*; its geometric model is shown in Figure 5. The vertical distance from the robot's centre point to the centreline L_{mid}.

Using the point-to-line distance formula, the lateral deviation of the robot from the navigation line can be expressed as:

$$d_{lat} = \frac{|A \cdot 0 + B \cdot 0 + C|}{\sqrt{A^2 + B^2}} = \frac{C}{\sqrt{A^2 + B^2}} \quad (4)$$

If $C > 0$ indicates that the navigation line is to the robot's left, the robot is veering to the right (where d_{lat} is positive); conversely, the robot is veering to the left *(Zhou et al., 2020)*. The heading deviation is the angle between the robot's current heading and the direction of the tree row. Since the direction vector of the tree row's linear equation is $(B, -A)$, the heading deviation ϕ_{err} is:

$$\varphi_{err} = \arctan\left(-\frac{A}{B}\right) \quad (5)$$

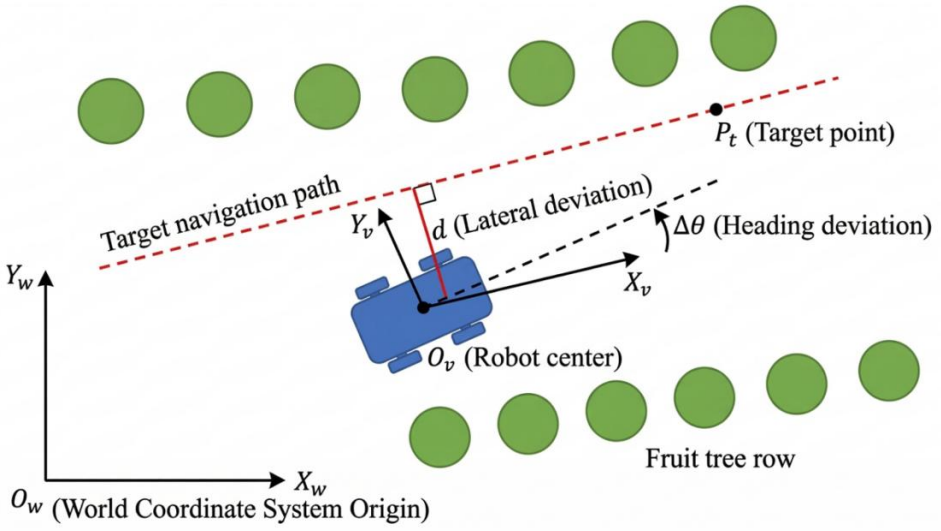

Fig. 5 – Geometric Solution Model for Relative Positioning Deviation

Adaptive Multi-Source EKF Fusion Framework

To address the issue of single-sensor failure in the complex environment of orchards, this study has developed a state-space model for multi-source heterogeneous data fusion based on the adaptive extended Kalman filter (EKF); the overall algorithmic architecture is shown in Figure 6.

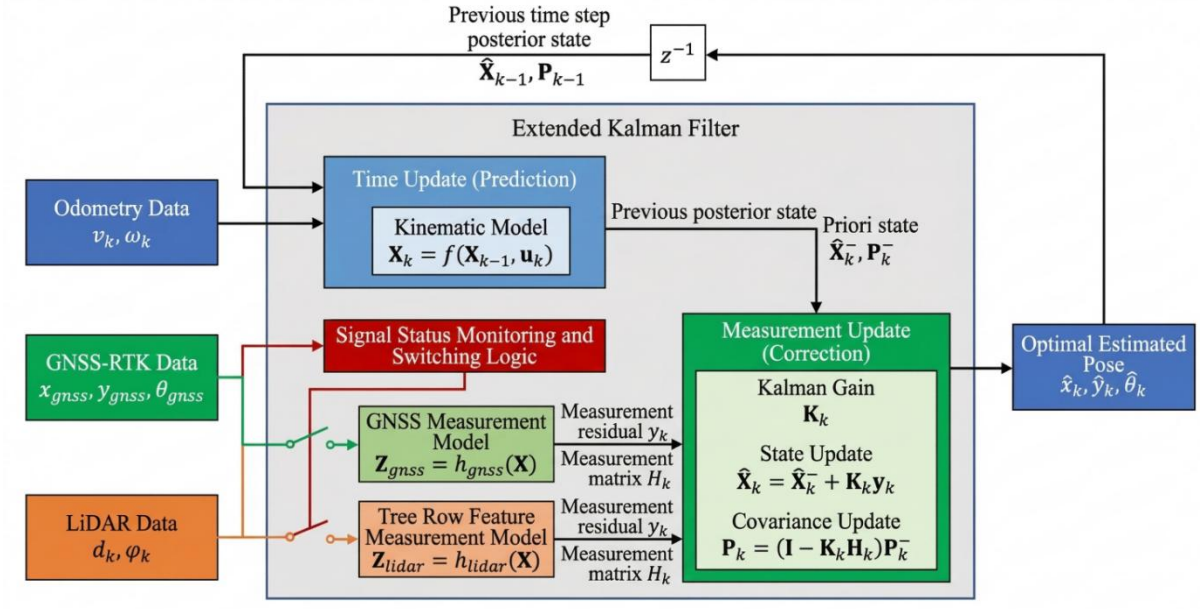

Fig. 6 – EKF algorithm architecture of the multi-source fusion positioning system

The navigation coordinate system is defined to be consistent with the established ENU local coordinate system *(Zhang et al., 2024)*; the origin of the robot's body coordinate system is defined as the geometric centre of the robot's chassis, with the X-axis pointing towards the front of the vehicle. The system's state vector X_k is defined as the robot's two-dimensional planar pose in the navigation coordinate system, namely:

$$X_k = [x_k, y_k, \theta_k]^T \quad (6)$$

Here, (x_k, y_k) represents the robot's planar position coordinates at time t_k, and θ_k denotes the yaw angle, with a range of$(-\pi, \pi)$.To improve the accuracy of the numerical integration, a second-order Runge-Kutta approximation is employed here, where by $\theta_{k-1} + \frac{1}{2}\omega_k \Delta t)$ is used in place of θ_{k-1} for the projection calculation *(Zhang et al., 2014)*. In the equation, W_{k-1} is the process noise vector, assumed to follow a Gaussian distribution with mean zero and standard deviation $W_{k-1} \sim N(0, Q_k)$.The process noise covariance matrix Q_k reflects the estimation uncertainty of the odometer under the influence of factors such as wheel slip and road irregularities; it is defined as follows:

$$Q_k = diag(\sigma_x^2, \sigma_y^2, \sigma_\theta^2) \quad (7)$$

Due to the non-linear nature of the kinematic model, standard EKF linearisation is applied to derive the state transition Jacobian matrix. The system fuses two types of heterogeneous observations. When in an open area, the GNSS-RTK provides absolute pose observations, and its observation matrix is a standard 3×3 identity matrix:

Conversely, when GNSS signals are degraded, the system relies on tree-row features extracted by LiDAR. The LiDAR observation vector $\mathrm{Z}_{\mathrm{lidar,k}}$ consists of the lateral deviation $\boldsymbol{d}_{\boldsymbol{l},\mathrm{k}}$ and heading deviation $\phi_{\boldsymbol{l},\mathrm{k}}$ relative to the tree row:

$$Z_{lidar,k} = \left[d_{L,k}, \phi_{L,k}\right]^T \quad (8)$$

The theoretical observation value corresponding to the predicted state is expressed as a non-linear function $h_{lidar}(\cdot)$, and standard linearisation is performed to compute its Jacobian matrix $H_{lidar,k}$ for EKF updates *(Zhang et al., 2022)*.

Adaptive compensation mechanism based on signal confidence

This system constructs the RTK signal confidence factor γ_k based on RTK status monitoring indicators. Let the RTK status flag be S_{rtk} (4 = Fixed, 5 = Float, others = Invalid), and the horizontal accuracy factor be H_{dop}. γ_k is defined as follows:

$$\gamma_k = \begin{cases} 1, & if S_{rtk} = 4 and H_{dop} < 1.5 (High\ confidence) \\ \eta \cdot H_{dop}, & if S_{rtk} = 5 (Moderate\ confidence) \\ \infty, & others (Low\ confidence) \end{cases} \quad (9)$$

In the equation, η is the penalty coefficient (with a value > 10), which is used to rapidly amplify the weight of the uncertainty associated with the floating solution. In the EKF update procedure, the observation noise covariance matrix R_k determines the filter's 'degree of confidence' in the observed data. This system dynamically constructs an adaptive covariance matrix $R^*_{gnss,k}$ based on γ_k:

$$R^*_{gnss,k} = \gamma_k^2 \cdot R_{gnss,0} = \begin{bmatrix} (\gamma_k \sigma_x)^2 & 0 & 0 \\ 0 & (\gamma_k \sigma_y)^2 & 0 \\ 0 & 0 & (\gamma_k \sigma_\theta)^2 \end{bmatrix} \quad (10)$$

In the equation, $R_{gnss,0}$ denotes the nominal noise variance matrix for the RTK fixed solution. Based on the penalty factor γ_k, the system's observation update logic switches adaptively between the following two modes:

1) Full-source fusion mode ($\gamma_k = 1$ (RTK Fixed)): this mode utilises H_{gnss} for observation updates, employing high-precision RTK data to correct the robot's full state (x, y, θ), whilst simultaneously calibrating the odometer's systematic bias online to eliminate previous cumulative drift and minimise the filter covariance matrix *(Zhong et al., 2020)*.

2) Geometric Constraint Compensation Mode ($\gamma_k > 1$ (RTK Float/Lost)): the filter stops using unstable GNSS data updates to prevent the track from being 'pulled off course'. The built-in H_{lidar} and the observed residual $\mathcal{Y}_{lidar}$ are then utilised to update the EKF. The compensation mechanism works as follows: the lateral deviation d in the observation equation constrains the robot's degrees of freedom perpendicular to the tree row, thereby eliminating drift in the y-axis (local) direction. Meanwhile, heading compensation is achieved by the angular deviation ϕ in the observation equation, which strongly constrains the robot's heading angle θ, thereby suppressing angular divergence.Through this strategy, the system utilises RTK correction in open areas and relies on tree rows to lock onto heading and lateral position in obstructed areas, thereby achieving robust positioning that relies on satellites at a macro level and on the environment at a micro level.

RESULTS

Vineyard Field Test

The reliability of field test data depends largely on the representativeness of the test environment and the stability of the hardware platform. This section provides a detailed overview of the characteristics of the selected orchard test site, as well as the configuration of the test platform built on the ROS architecture. When selecting a location for autonomous operation of orchard inspection robots, it is necessary to ensure that the area is free of obstacles in order to guarantee stable positioning signals. The project has selected a grape-growing site, as shown in Figure 7. This demonstration site employs a standardised cultivation model, with rows spaced approximately 3 metres apart and plants spaced approximately 1.5 metres apart; each planting strip extends for up to 400 metres, providing an ideal testing environment for the robot navigation system.

Fig. 7 – Vineyard scenery

In orchard operations, the accuracy of path tracking is directly linked to the measurement performance of the positioning receiver. To assess the stability and reliability of the equipment, static positioning accuracy tests must be conducted prior to commencing formal operations. The specific procedure is as follows: select an unobstructed test area with a clear line of sight, keep the mobile robot stationary, activate the dual-antenna GNSS-RTK positioning system, and set the data sampling rate to 10 Hz.

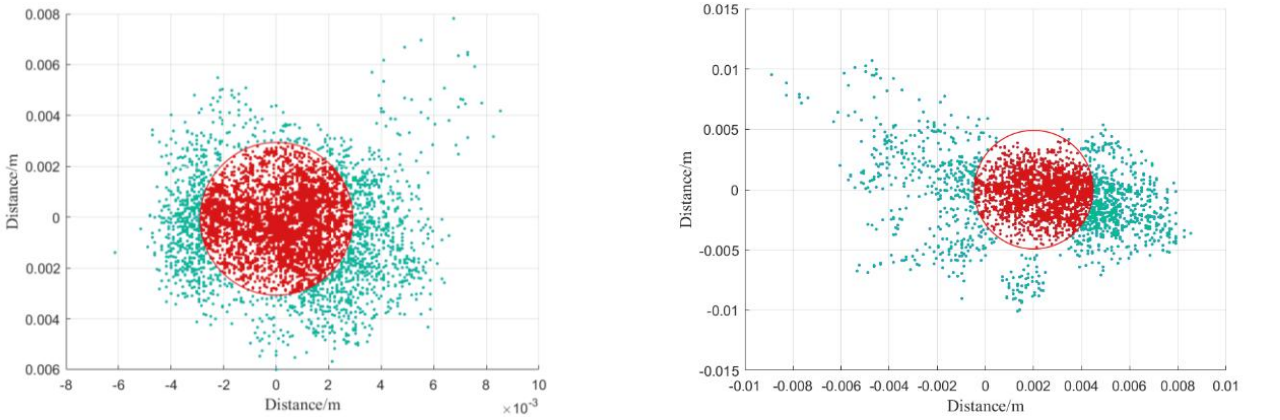

（a）Static RTK data in open terrain （b）Static RTK data collected within a vineyard environment

Fig. 8 – RTK data collection experiment

The results of the positioning performance tests indicate that, based on 100 sets of GNSS-RTK positioning data samples, the positioning accuracy is as shown in Figure 8. Statistical data show that the horizontal positioning accuracy is within 1 cm and the vertical positioning error is within 2 cm, thereby meeting the technical requirements for positioning in autonomous navigation operations within orchards.

To evaluate the accuracy of the inter-row localisation algorithm, this study designed a test in which the robot autonomously navigated along the centreline of a standard 50-metre-long vine row at a speed of 1.0 m/s, utilising a high-precision RTK-GNSS rover to record the robot's absolute position coordinates (x_{rtk}, y_{rtk}) and heading angle θ_{rtk}.

Using a pre-calibrated map coordinate system transformation matrix, the RTK data is projected onto the current local coordinate system of the tree row, and the true lateral deviation $e_{y\_gt}t$ and heading deviation $e_{\theta\_gt}t$ are calculated to serve as evaluation benchmarks.

To verify the robustness of the algorithm, the experimental path included two natural gaps in the vineyard, where 1 to 2 grapevines were missing in succession (with gap lengths of approximately 1.5 m to 3.0 m). This is a critical scenario for testing whether the localisation algorithm drifts due to the loss of features.

Figure 9 records the curve showing the variation in LiDAR-estimated pose error over distance travelled during a complete in-row navigation run by the robot.

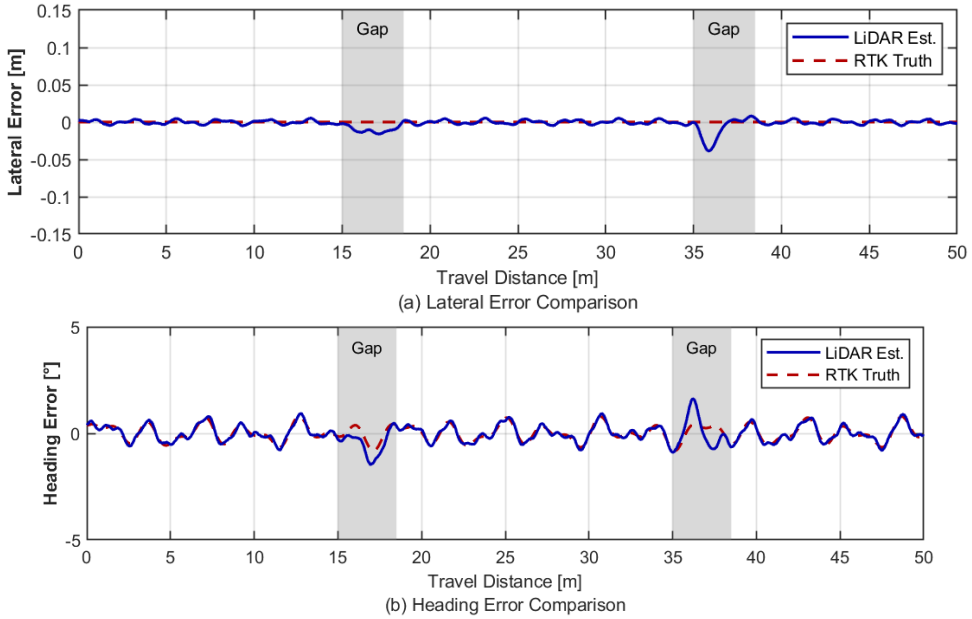

Fig. 9 – Comparison of Lidar Relative Positioning Error with RTK True Values

The results show that the positioning curves estimated by LiDAR closely match the RTK reference curves. In sections where the vines are evenly distributed, the lateral error is minimal and stable; in areas with gaps in the vine rows, the positioning error exhibits brief fluctuations but does not diverge or undergo sudden jumps. Once the vehicle exits these gaps, the error rapidly converges back to normal levels.

In order to evaluate the system's performance more comprehensively, the root mean square error, mean absolute error and maximum error were calculated from the experimental data collected over multiple trials. The results are summarised in Table 1.

Table 1

Statistical Comparison of Trajectory Tracking Errors

Evaluation Criteria	Root Mean Square Error	Mean Absolute Error	Maximum Error
Lateral deviation	0.042 m	0.035 m	0.098 m
Course deviation	1.85°	1.42°	3.75°

The root mean square error for lateral positioning throughout the entire process is just 4.2 cm. In an operational scenario with a row spacing of 3 m, this means that the safety margins on both sides of the robot are significantly greater than the positioning error, which is sufficient to ensure that no collisions occur during long-term operation. The root mean square error for heading angle is kept within 2°. For a dual-loop PID control system, this level of precision indicates that the state variables provided by the perception layer are of extremely high quality.

In summer testing scenarios, the dense foliage of vineyards acts as a natural signal blocker, resulting in severe GNSS multipath effects; RTK receivers frequently experience reduced positioning accuracy or signal interruptions. Figure 10 illustrates the track performance during multi-row operations in a circular pattern during the summer.

As shown in the figure, during the straight-line inspection phase, when the robot enters an area with dense tree canopy cover, the raw GNSS-RTK positioning data not only exhibits random lateral jumps of approximately 0.03 m, but also demonstrates a continuous decline in accuracy and signal instability.

If the system relied solely on satellite navigation, this high-frequency positioning noise and persistent drift would be directly fed into the lower-level controller, causing the tracked chassis to make frequent, ineffective steering adjustments, which could lead to vehicle vibrations or even significant cumulative yaw over long distances.

Upon detecting this anomaly, the integrated positioning system described in this paper rapidly and smoothly reduces the confidence weighting of the satellite data, shifting the primary responsibility to tree-row feature matching positioning based on 3D LiDAR. Quantitative data indicate that during a weak-signal navigation phase lasting up to 25 seconds, the system's average lateral tracking error (RMSE) remained stable at 0.10 m, effectively suppressing persistent drift and perfectly bridging the satellite signal blind spot.

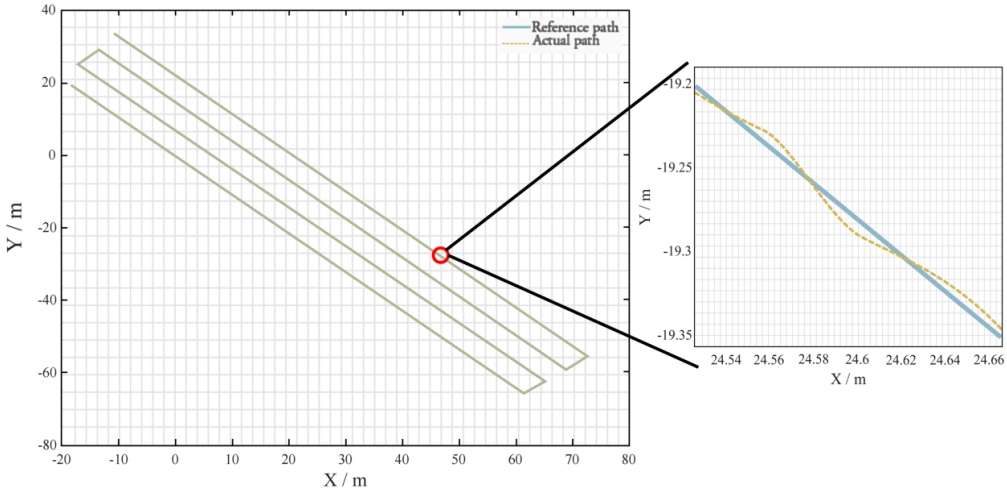

Fig. 10 – Summer Navigation Trajectory Map

CONCLUSIONS

To address the limitations of single-sensor positioning in unstructured orchards due to canopy obstruction and complex terrain, this study proposes an adaptive extended Kalman filter (EKF)-based fusion method combining GNSS-RTK and 3D LiDAR. By employing an improved RANSAC algorithm for map-less tree-row fitting, the system reliably extracts lateral and heading geometric constraints despite severe environmental interferences like weeds and muddy ruts. Furthermore, a dynamic covariance adjustment mechanism based on RTK signal confidence enables seamless transitions to LiDAR-based compensation during satellite signal degradation, effectively mitigating odometer drift. Field experiments in vineyards demonstrate highly robust, centimeter-level accuracy, with lateral and heading root mean square errors (RMSE) restricted to 0.042 m and 1.85°, respectively. However, certain limitations remain, such as potential performance degradation in highly irregular orchards lacking distinct structural constraints, and the computational burden of continuous 3D LiDAR processing. To address this computational bottleneck, future research will explore advanced point cloud preprocessing pipelines, incorporating semantic segmentation, noise filtering, and adaptive downsampling, to optimize tree-row data extraction and significantly reduce computational overhead. Despite these challenges, this highly reliable state estimation framework effectively overcomes "blind-spot localization" issues, establishing a solid foundation for future research on map-free global path planning and dynamic obstacle avoidance in agricultural robotics.

REFERENCES

[1] Gao P., Jiang J., Song J. (2021). Fruit Tree Model Reconstruction Method for Robotic Canopy Volume Measurement in Orchards. *IEEE Access.* vol. 9, pp.156246–156259.

[2] Jiang H., Pi J., Li A., Yin C. (2022). Dynamic Local Path Planning for Intelligent Vehicles Based on Sampling Area Point Discrete and Quadratic Programming. *IEEE Access*, vol. 10, pp.70279-70294.

[3] Lv P., Li Z. (2025). Research on Yolov5-Based Visual Slam Optimisation Method in Farm Depot Environment. *INMATEH-Agricultural Engineering*. 75(1). 83-94. DOI: https://doi.org/10.35633/inmateh-75-07

[4] Nie F., Zhang W., Wang Yl. (2021). A forest 3-d lidar slam system for rubber-tapping robot based on trunk center atlas. *IEEE/ASME Trans. on Mechatronics*. 27(5): 2623-2633.

[5] Pire T., Fischer T., Castro G., De Cristóforis P., Civera J., Berlles J. (2017). S-PTAM: Stereo parallel tracking and mapping. *Robot. Auton. Syst*. 93, 27–42.
[6] Qin Z., Wang H., Lv P. (2024). Research on Simultaneous Localization and Mapping Method for Orchards Based on Scan Context and NDT-ICP Fusion Scheme. *INMATEH-Agricultural Engineering*. 73(2). 636-646. DOI: https://doi.org/10.35633/inmateh-73-54
[7] Qiu Z., Zhao N., Zhou L., Wang M., Yang L., Fang H., Liu Y. (2020). Vision-based moving obstacle detection and tracking in paddy field using improved yolov3 and deep SORT. *Sensors*, 20(15), 4082.
[8] Rösmann C., Hoffmann F., Bertram T. (2015). Timed-elastic-bands for time-optimal point-to-point nonlinear model predictive control. In *Proceedings of the 2015 European Control Conference (ECC)*, Linz, Austria, 15–17 July. 3352–3357.
[9] Shan T., Englot B. (2018). LeGO-LOAM: Lightweight and ground-optimized lidar odometry and mapping on variable terrain. *IEEE/RSJ International Conference on Intelligent Robots and Systems (IROS)*. 4758-4765.
[10] Wu, J., Ma, X., Peng, T., Wang, H. (2021). An improved timed elastic band (TEB) algorithm of autonomous ground vehicle (AGV) in complex environment. *Sensors*, 21(24), 8312.
[11] Xue G., Li R., Zhang Z. (2023). Research Status and Development Trend of SLAM Algorithm Based on 3D LiDAR (基于 3D 激光雷达的 SLAM 算法研究现状与发展趋势). *Information and Control*, vol. 52, Issue (01): 18-36.
[12] Yang, L., Xu, Y., Liang, Y., Qin, J., Li, Y., Wang, X., Wu, C. (2022). Extraction of straight field roads between farmlands based on agricultural vehicle-mounted LiDAR. *International Journal of Agricultural and Biological Engineering*, 15(5), 155-162.
[13] Yang, J., Chung, S. J., Hutchinson, S., Johnson, D., Kise, M. (2015). Omnidirectional-vision-based estimation for containment detection of a robotic mower. In *2015 IEEE International Conference on Robotics and Automation (ICRA)*. pp. 6344-6351.
[14] Zhou K., Leck Jensen A., Sørensen C G l. (2014). Agricultural operations planning in fields with multiple obstacle areas. *Computers and Electronics in Agriculture*. 109, 12-22.
[15] Zhang Y., Mo Z., Tian H. (2024). Path planning algorithm of agricultural robot based on improved APF-FMT*. *Journal of South China Agricultural University*. 45(3): 408-415.
[16] Zhou Z., Cao J., Di S. (2021). Overview of 3D LiDAR SLAM algorithms (3D 激光雷达 SLAM 算法综述). *Chinese Journal of Scientific Instrument*, vol. 42, Issue (09): 13-27.
[17] Zhang J., Singh S. (2014) LOAM: Lidar odometry and mapping in real-time. Robotics: *Science and Systems Conference*. 2(9): 1-9.
[18] Zhang, X., Zhu, T., Du, L., Hu, Y., Liu, H. (2022). Local path planning of autonomous vehicle based on an improved heuristic Bi-RRT algorithm in dynamic obstacle avoidance environment. *Sensors*, 22(20), 7968.
[19] Zhong, X., Tian, J., Hu, H., Peng, X. (2020). Hybrid path planning based on safe A* algorithm and adaptive window approach for mobile robot in large-scale dynamic environment. *Journal of Intelligent & Robotic Systems*, 99(1), 65-77.
[20] Zhou, X., Wang, Z., Ye, H., Xu, C., Gao, F. (2020). Ego-planner: An ESDF-free gradient-based local planner for quadrotors. *IEEE Robotics and Automation Letters*, 6(2), 478-485.